

Helical Fermi Arc in Altermagnetic Weyl Semimetal

Yu-Hao Wan,¹ Cheng-Ming Miao,¹ Peng-Yi Liu,¹ and Qing-Feng Sun^{1, 2, *}

¹*International Center for Quantum Materials, School of Physics, Peking University, Beijing 100871, China*

²*Hefei National Laboratory, Hefei 230088, China*

We investigate the topological properties of modified Dirac Hamiltonians with an altermagnetic mass term and reveal a novel mechanism for realizing altermagnetic Weyl semimetals. Unlike the conventional Wilson mass, the altermagnetic mass drives direct transitions between nontrivial Chern phases of opposite sign and fundamentally reshapes the band inversion surface. By extending this framework to three dimensions, we construct a minimal lattice model that hosts pairs of Weyl nodes as well as coexisting helical Fermi arcs with opposite chirality on the same surface, which is a phenomenon not found in conventional magnetic Weyl semimetals. We further propose a practical scheme to realize these phases in multilayer structures of 2-dimensional Rashba metal with engineered d -wave altermagnetic order. Our results deepen the theoretical understanding of mass terms in Dirac systems and provide concrete guidelines for the experimental detection and realization of altermagnetic Weyl semimetals.

I. INTRODUCTION

Weyl semimetals (WSMs) are gapless three-dimensional topological phases characterized by isolated band-touching points known as Weyl nodes, which act as quantized monopoles of Berry curvature [1, 2]. Realizing WSM phases typically involves breaking either inversion (\mathcal{P}) [3–5] or time-reversal (\mathcal{T}) [6, 7] symmetry, positioning magnetism as a natural and experimentally accessible route to achieve and control these states. To date, most of the magnetic WSMs rely on ferromagnetic [7–10] or antiferromagnetic [11, 12] order, whose net or staggered magnetization explicitly breaks \mathcal{T} , producing characteristic responses such as anomalous Hall effects [7, 11, 13–15], chiral anomalies [14, 16–20], and surface Fermi-arc states [1, 21–23].

A newly recognised form of collinear order, altermagnetism, now enlarges this landscape [24–27]. An altermagnet has zero net magnetization yet still breaks \mathcal{T} symmetry in momentum space, generating significant spin splittings strongly dependent on crystal symmetry [28, 29]. The unique properties of altermagnets have attracted substantial theoretical and experimental attention due to their potential for unconventional spintronic effects [30–32], anomalous transport phenomena [24, 33–41], and novel superconducting effects [29, 42–47]. However, the impact of altermagnetism on Weyl physics remains largely unexplored. In particular, can altermagnetic order stabilize Weyl phases distinct from those realized in ferromagnetic or antiferromagnetic systems?

To address this, it is essential to understand how different mass terms in the modified Dirac equation shape the topological phases of both two- and three-dimensional systems [48]. While most studies have focused on the interplay between the uniform Dirac mass and the quadratic Wilson mass [49–51], recent work suggests that symmetry-allowed d -wave altermagnetic mass

terms may fundamentally alter the topological phase diagram[52], enabling novel WSM phases with properties absent in ferromagnetic or antiferromagnetic systems.

In this work, we show that combining Dirac and altermagnetic masses indeed yields a distinct class of Weyl semimetal. Using a minimal square-lattice model we demonstrate that Weyl nodes arise precisely where the two masses cancel, and that their arrangement differs qualitatively from the Wilson-mass case. Most strikingly, the resulting phase hosts two counter-propagating Fermi arcs on the same surface, forming a helical surface channel absent in conventional magnetic WSMs. We then propose a multilayer structure, where two-dimensional metallic layers with d -wave altermagnetic order and alternating Rashba spin-orbit coupling are stacked with insulating spacers. This setup naturally realizes the required mass structure and offers a platform for studying the predicted effects. Our findings reveal a new route to engineer and control unconventional topological phases through altermagnetism, opening up opportunities for observing exotic surface states and transport phenomena beyond those of traditional magnetic Weyl semimetals.

The rest of the paper is organized as follows. In Sec. II, we analyze the differences between Wilson and altermagnetic masses in the two-dimensional modified Dirac equation, highlighting their distinct topological implications. In Sec. III, we extend the model to three dimensions and demonstrate how the interplay between the Dirac and altermagnetic masses gives rise to altermagnetic Weyl semimetals with helical fermi arc surface states. In Sec. IV, we propose and analyze the multilayer heterostructure and map out the corresponding topological phase diagram. Finally, we summarize our findings in Sec. V.

* Corresponding author: sunqf@pku.edu.cn

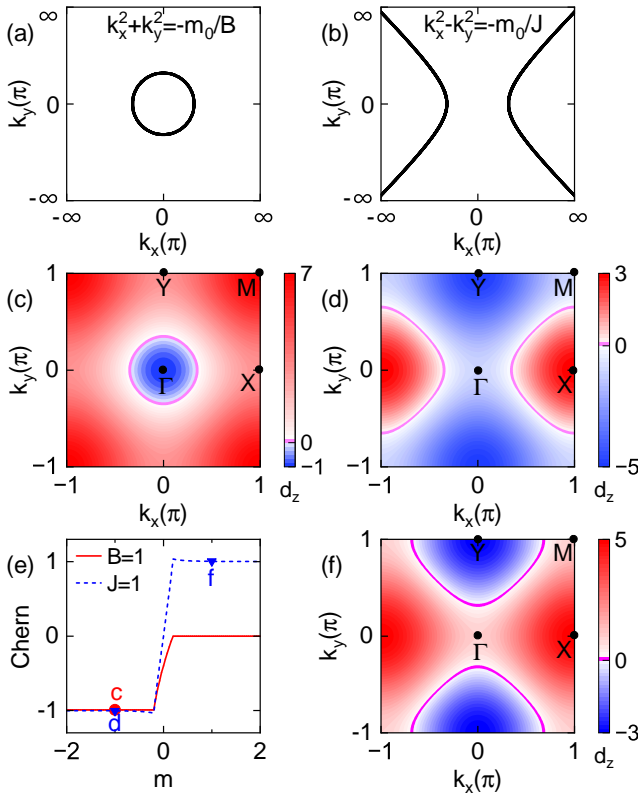


FIG. 1. (a) BIS for the Dirac mass and Wilson mass in the continuum model. (b) BIS for the Dirac mass and altermagnetic mass in the continuum model. (c) BIS for the Dirac mass and Wilson mass in the lattice model, with $m_0 = -1$ and $J = 1$; color indicates the d_z component. (d) BIS for the Dirac mass and altermagnetic mass in the lattice model, with $m_0 = -1$ and $J = 1$. (e) Chern number as a function of Dirac mass m_0 for altermagnetic mass (blue line) and Wilson mass (red line); the three points marked c, d, and f correspond to different d_z distributions in the Brillouin zone in the panels (c, d, and f). (f) BIS for the Dirac mass and altermagnetic mass in the lattice model, with $m_0 = 1$ and $J = 1$.

II. TOPOLOGICAL EFFECTS OF DIRAC, WILSON, AND ALTERMAGNETIC MASS TERMS

The rich topological structure of WSMs can be traced back to their deep connection with Chern insulators. In particular, the modified Dirac Hamiltonian provides a universal minimal description of band topology and topological phase transitions in both two- and three-dimensional systems. The key physics is encoded in the mass term $M(\mathbf{k})$, whose precise form determines the nature of the band inversion and the topological classification.

Most studies have focused on the interplay between a constant Dirac mass and a quadratic Wilson mass, but recent advances in altermagnetic systems suggest that an alternative quadratic mass term—associated with d -

wave altermagnetic order—may fundamentally reshape the topological phase diagram. To clarify these distinctions and motivate our construction of altermagnetic Weyl semimetals, we systematically compare the topological effects of Dirac, Wilson, and altermagnetic mass terms using the 2D modified Dirac model. In two dimensions, the minimal model is given by

$$H(\mathbf{k}) = v_F(k_x\sigma_x + k_y\sigma_y) + M(\mathbf{k})\sigma_z, \quad (1)$$

where v_F is the Fermi velocity, $\sigma_{x,y,z}$ are the Pauli matrices in the spin space, and $\mathbf{k} = (k_x, k_y)$ is the crystal momentum. The mass term $M(\mathbf{k})$ is central to determining the topological nature of the system.

For the modified Dirac equation, the mass term typically contains a constant Dirac mass m_0 and a quadratic Wilson mass $B(k_x^2 + k_y^2)$, where B is the Wilson mass parameter [53–55]. The interplay between the Dirac mass m_0 and the Wilson mass B governs the system's topological phase when the product $m_0B < 0$, the model describes a nontrivial Chern insulator, while $m_0B > 0$ results in a trivial insulator [48, 49]. The transition point corresponds to a band inversion, where the energy gap closes and reopens as the sign of m_0 or B changes.

Recently, motivated by the physics of d -wave altermagnetic order, another type of quadratic mass term has been considered [28, 29, 34, 52]

$$M_S(k_x, k_y) = J(k_x^2 - k_y^2), \quad (2)$$

where J is the strength of the altermagnetic ordering. Like the Wilson mass, this term is quadratic in momentum and couples to σ_z , but it breaks rotational symmetry, introducing a sign change between the k_x and k_y directions.

To illustrate the fundamental difference between these two mass terms, we examine the geometry of the band inversion surface (BIS), defined as the set of momentum points where the mass term vanishes and the bulk gap closes. For the Dirac equation with a Wilson mass, the BIS is determined by $k_x^2 + k_y^2 = -m_0/B$, forming a circle centered at the origin [see Fig. 1(a)]. In contrast, for the Dirac equation with an altermagnetic mass, the BIS is given by $k_x^2 - k_y^2 = -m_0/J$, which represents a hyperbola [see Fig. 1(b)]. These distinct BIS geometries reflect the underlying symmetry of each mass term and dictate different mechanisms for gap closing and topological phase transitions.

These geometric differences in the BIS have profound topological implications. The circular BIS associated with the Wilson mass supports a well-defined Chern number in the continuum, as the mass term maintains a uniform sign at infinity. In contrast, the altermagnetic mass leads to a non-uniform mass sign at large momenta, so the mapping from momentum space to the Bloch sphere fails to close, rendering the Chern number ill-defined in the pure continuum limit.

To rigorously define topological invariants, we regularize the model on a lattice, where the Brillouin zone is

compact. On the square lattice, the Wilson mass term takes the form $m_0 - 2B(\cos k_x + \cos k_y - 2)$. Setting $B = 1$, we compute the Chern number as a function of m_0 . As shown in Fig. 1(e), the Chern number changes from -1 ($m_0 < 0$) to 0 ($m_0 > 0$), reflecting a topological phase transition driven by the sign reversal of the Dirac mass. Correspondingly, the BIS for the Wilson mass is a closed loop centered at the Γ point in the Brillouin zone [see Fig. 1(c)].

For the altermagnetic mass, the lattice regularization yields $2J(\cos k_y - \cos k_x)$, and we set $J = 1$ for comparison. In this case, as m_0 varies from -1 to 1 , the Chern number switches from -1 to 1 [Fig. 1(e)], but the system never enters a trivial phase. Correspondingly, the BIS evolves from an open hyperbolic contour in the continuum limit to a closed loop on the lattice. This closure arises because the compact, periodic nature of the Brillouin zone effectively wraps the open hyperbolic branches of the continuum model, forcing them to connect and form a closed loop. Specifically, the BISs for $m_0 = -1$ and $m_0 = 1$ form closed loops around the X and Y points, respectively [Fig. 1(d,f)]. According to recent theoretical advances in Chern number classification based on high-symmetry points [56], these two phases can be labeled as $C_X = -1$ and $C_Y = +1$, indicating that the topological charge is concentrated at different points in the Brillouin zone. We also discuss in the Appendix the form factors of other altermagnetic orders. There we show that the sign reversal of the Dirac mass similarly drives a change in the Chern-number sign, accompanied by a transfer of the topological charge between different high-symmetry points in the Brillouin zone.

In summary, Wilson and altermagnetic mass terms produce fundamentally different effects when the Dirac mass changes sign. For the Wilson mass, changing the Dirac mass sign drives a transition between trivial and nontrivial Chern insulator phases, with the Chern number switching from -1 to 0 via a band inversion at the Γ point. In contrast, for the altermagnetic mass, reversing the Dirac mass sign causes the Chern number to switch directly between two nontrivial values of opposite sign, relocating the topological charge between different high-symmetry points without passing through a trivial phase. This unique transition mechanism imparts distinctive properties to altermagnetic Weyl semimetals, motivating the following introduction of a minimal altermagnetic Weyl model.

III. MINIMAL TWO BANDS MODEL FOR ALTERMAGNETIC WEYL SEMIMETAL

The close connection between 2D Chern insulators and 3D Weyl semimetals provides a natural route to generalize the modified Dirac equation to three dimensions. By promoting the Dirac mass in the 2D Dirac equation to a k_z -dependent function, the 3D system can be viewed as a series of 2D slices at fixed k_z , each described by

a 2D Hamiltonian with a k_z -dependent Dirac mass. In this framework, as k_z is varied, the Chern number associated with each slice may change, and Weyl nodes emerge at those critical k_z where the gap closes, signaling topological phase transitions between different 2D Chern phases. Crucially, when the 2D model includes an altermagnetic mass term, the interplay between the altermagnetic and Dirac masses produces a novel topological structure unique to the altermagnetic Weyl semimetal.

Motivated by this picture, we construct the following minimal lattice Hamiltonian for an altermagnetic Weyl semimetal

$$H_{\min}(\mathbf{k}) = A \sin(k_x) \sigma_x + A \sin(k_y) \sigma_y + [m_0 + 2J(\cos k_y - \cos k_x) + \cos k_z] \sigma_z, \quad (3)$$

where m_0 is the Dirac mass parameter and J controls the strength of the altermagnetic mass. In our calculations, we take the parameters $A = 1$, $m_0 = 0$, and $J = 1$. Here, the Dirac mass is explicitly modified to depend on k_z via the term $(m_0 + \cos k_z) \sigma_z$, directly extending the 2D modified Dirac equation with altermagnetic mass to three dimensions. This construction captures the essential features of altermagnetic Weyl semimetals, including the unique interplay between the k_z -dependent Dirac mass and the altermagnetic mass term.

The hallmark of Weyl semimetals is the existence of topologically protected surface states known as Fermi arcs, which connect the projections of Weyl nodes of opposite chirality in the surface Brillouin zone [1, 2]. To explicitly demonstrate these unique surface features and reveal how they are modified by the altermagnetic mass, we discretize the x direction into $N = 50$ lattice sites and compute the energy spectrum $E(k_y)$ as a function of k_z . Fig. 2(a1–a5) show representative spectra at $k_z = -\pi, -\pi/2, 0, \pi/2, \pi$, where each eigenstate is color-coded by its average position $\langle x \rangle$ to highlight its spatial character. States localized near the edges correspond to surface states. Remarkably, for $|k_z| < \pi/2$, Fermi arcs are found near $k_y = \pm\pi$, corresponding to chiral surface states at the boundaries in the x direction. For $|k_z| > \pi/2$, the Fermi arcs shift to $k_y = 0$, with their chirality reversed. The chirality of these Fermi arc surface states is identified by the direction of the group velocity surface states localized at opposite edges propagate in opposite directions, as determined by the slope of their energy dispersion. Unlike conventional Weyl semimetals, the altermagnetic Weyl semimetal supports coexisting surface states with opposite chirality on the same surface. This coexistence of counter-propagating Fermi arcs is a hallmark of the altermagnetic Weyl phase, and originates from the interplay between the altermagnetic mass and the Dirac mass. Specifically, a sign reversal of the Dirac mass leads to a change in the Chern number, which in turn produces Fermi arcs of opposite chirality.

To further clarify the topological origin of the surface states, we analyze the Chern number of the two-dimensional Hamiltonian $H_{\min}(k_x, k_y, k_z)$ as a function of k_z . For each fixed k_z , this Hamiltonian reduces to a

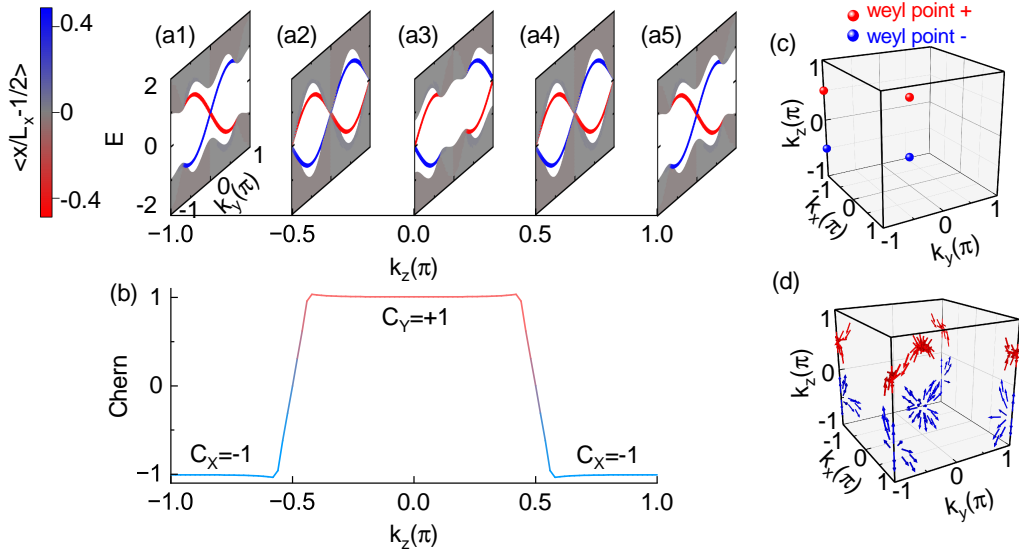


FIG. 2. (a1–a5) Slab energy spectra as a function of k_z in the Weyl semimetal phase, with eigenstates color-coded according to their average position $\langle x \rangle$ to distinguish surface and bulk states. (b) The corresponding Chern number $C(k_z)$ for each fixed k_z slice. (c) Distribution of Weyl nodes in the Brillouin zone, with Fermi arcs connecting pairs of nodes. (d) Berry curvature distribution in the Brillouin zone, highlighting regions of concentrated topological charge.

2D modified Dirac model with an altermagnetic mass, as discussed in Sec. II. As illustrated in Fig. 2(b), the surface Fermi arcs arise from two distinct Chern insulating phases with different Chern numbers in the 2D Brillouin zone. As k_z varies, a topological phase transition occurs at $|k_z| = \pi/2$: for $|k_z| < \pi/2$, the BIS encloses the X point, corresponding to a Chern number $C_X = -1$; for $|k_z| > \pi/2$, the BIS encloses the Y point, and the Chern number switches to $C_Y = +1$ [56]. This sharp change in Chern number is a direct manifestation of the interplay between the Dirac mass and the altermagnetic mass. The transition points $k_z = \pm\pi/2$ mark the locations of the Weyl nodes, situated at $(k_x, k_y) = (0, 0)$ and (π, π) in the $k_x - k_y$ plane [see Fig. 2(c)]. Importantly, we find that the Fermi arc connecting the two Weyl points at $(0, 0, \pm\pi/2)$ exhibits chirality opposite to that of the arc connecting $(-\pi, -\pi, \pm\pi/2)$. This opposite chirality of the fermi arcs is evident from both the Chern number calculations and the surface state dispersions shown in Fig. 2(b).

To confirm the bulk–boundary correspondence discussed above, we computed the Berry-curvature distribution of the lower band over the entire Brillouin zone, using a dense 200^3 momentum grid [Fig. 2(d)]. For a generic two-band Hamiltonian $H(\mathbf{k}) = \mathbf{d}(\mathbf{k}) \cdot \boldsymbol{\sigma}$, the Berry

curvature reads [48]:

$$\boldsymbol{\Omega}(\mathbf{k}) = \frac{1}{2} \frac{\mathbf{d}(\mathbf{k})}{|\mathbf{d}(\mathbf{k})|^3} \cdot (\partial_{k_x} \mathbf{d} \times \partial_{k_y} \mathbf{d}), \quad (4)$$

which we evaluate numerically by finite differences. The curvature is strongly peaked at the four Weyl nodes: positive monopoles at $(0, 0, \pi/2)$ and $(-\pi, -\pi, \pi/2)$, and negative monopoles at $(0, 0, -\pi/2)$ and $(-\pi, -\pi, -\pi/2)$. Integrating $\Omega_z(\mathbf{k})$ over each constant- k_z slice reproduces the slice Chern numbers obtained analytically, namely $C = +1$ for $|k_z| < \pi/2$ and $C = -1$ for $|k_z| > \pi/2$. This agreement provides a direct bulk confirmation of the topological phase transition driven by the interplay between the Dirac and altermagnetic mass terms.

IV. MULTILAYER REALIZATION OF ALTERMAGNETIC WEYL SEMIMETAL

To illustrate that the same mass–interplay mechanism can arise in a completely different setting, we consider a synthetic multilayer of two-dimensional d -wave altermagnetic metals. As sketched in Fig. 3(a), neighbouring layers are engineered to have opposite Rashba spin-orbit coupling strengths $+\lambda$ and $-\lambda$, while thin insulating spacers suppress direct hopping beyond nearest neighbours along z [6].

In momentum space the stack Hamiltonian is described by (lattice constant is set to unity)

$$H(\mathbf{k}_{\parallel}) = \sum_{i,j} c_{\mathbf{k}_{\parallel},i}^\dagger \left[-t(\cos k_x + \cos k_y) \sigma_0 \tau_0 \delta_{ij} + \lambda \tau_z (\sin k_x \sigma_x + \sin k_y \sigma_y) \delta_{ij} + J(\cos k_y - \cos k_x) \sigma_z \tau_0 \delta_{ij} \right. \\ \left. + \Delta_S \sigma_0 \tau_x \delta_{ij} + \frac{\Delta_D}{2} \sigma_0 (\tau_+ \delta_{j,i+1} + \tau_- \delta_{j,i-1}) \right] c_{\mathbf{k}_{\parallel},j}, \quad (5)$$

Here $c_{\mathbf{k}_{\parallel},i}^\dagger$ creates an electron with in-plane momentum $\mathbf{k}_{\parallel} = (k_x, k_y)$ in layer i ; σ_α act on real spin, whereas τ_α act on the layer degree of freedom and $\tau_{\pm} = (\tau_x \pm i\tau_y)/2$. The first term is the isotropic kinetic energy. The λ term encodes the layer-alternating Rashba spin-orbit coupling, which can naturally arise in a multilayer structure due to opposite electrostatic potential gradients at the top and bottom surfaces of each metallic layer, resulting in opposite Rashba spin-orbit coupling for adjacent layers. As a practical note, a similar Rashba-type spin texture can also be realized in thin films of three-dimensional topological insulators, whose top and bottom surfaces possess opposite spin orientations; when coupled to altermagnetic layers, such TI films can effectively provide the alternating Rashba coupling $(+\lambda, -\lambda)$ required in our multilayer structure. The J term is the d -wave altermagnetic exchange, which can be realized in materials such as RuO_2 [57] and $\text{KV}_2\text{Se}_2\text{O}$ [58] where momentum-dependent spin splitting has been observed in recent ARPES measurements. The last two terms describe, respectively, intra-cell hybridisation (Δ_S) and inter-cell hopping (Δ_D) along z . After Fourier transforming in the stacking direction, Δ_S and Δ_D combine into a k_z -dependent mass, $m(k_z) = \Delta_S - \Delta_D \cos k_z$.

It is convenient to block-diagonalize the Hamiltonian by a unitary transformation

$$U = \exp \left(i \frac{\pi}{4} \sigma_z \tau_z \right). \quad (6)$$

This transformation mixes the spin and pseudospin sectors such that

$$U \tau_{\pm} U^\dagger = \sigma_z \tau_{\pm}. \quad (7)$$

Physically, this rotates the basis so that the coupling between layers, which encoded in τ_{\pm} terms, becomes an effective σ^z term in each block. After applying U , the Hamiltonian decouples into two 2×2 blocks. The transformed Hamiltonian can be written as

$$\mathcal{H}'(\mathbf{k}) = -t(\cos k_x + \cos k_y) \sigma_0 + \lambda(\sin k_x \sigma_x + \sin k_y \sigma_y) \\ + \left[J(\cos k_y - \cos k_x) + \hat{\Delta}(k_z) \right] \sigma_z, \quad (8)$$

where $\hat{\Delta}(k_z)$ can be replaced by its eigenvalues $\pm \Delta(k_z)$, with

$$\Delta(k_z) = \sqrt{\Delta_S^2 + \Delta_D^2 + 2 \Delta_S \Delta_D \cos(k_z d)}. \quad (9)$$

where d is the superlattice period along the growth (z) direction. We have thereby reduced the problem to a

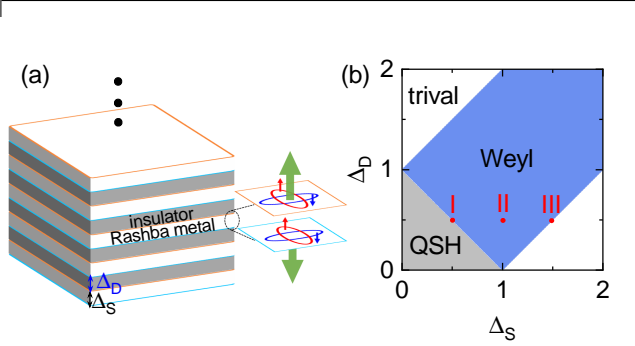


FIG. 3. (a) Schematic illustration of the proposed altermagnetic multilayer: two-dimensional metallic layers with d -wave altermagnetic order are stacked along z , and adjacent layers carry Rashba spin-orbit couplings of opposite sign $(+\lambda, -\lambda)$, as shown by the large green arrows. Thin insulating spacers suppress further-neighbour hopping, while intra-cell hybridization Δ_S and inter-cell tunnelling Δ_D are indicated. (b) Topological phase diagram as a function of the altermagnetic mass J and tunneling parameters Δ_S, Δ_D . The diagram highlights the regions corresponding to the trivial insulator, Weyl semimetal, and QSH phases. The three points (labeled I, II, III) indicate parameter sets used for the subsequent bulk and edge calculations, with specific values $(\Delta_S, \Delta_D) = (0.5, 0.5)$ for I, $(1, 0.5)$ for II, and $(1.5, 0.5)$ for III. In all calculations, we set $t = 0.1$, $\lambda = 0.5$, and $J = 0.5$.

family of 2×2 Bloch Hamiltonians parameterized by k_z , each of the form

$$H_{2D}(k_x, k_y; k_z) = -t(\cos k_x + \cos k_y) \sigma_0 + \lambda(\sin k_x \sigma_x + \sin k_y \sigma_y) + M(\mathbf{k}) \sigma_z, \quad (10)$$

with an effective mass term

$$M(\mathbf{k}) = J(\cos k_y - \cos k_x) \pm \Delta(k_z). \quad (11)$$

This 2×2 Hamiltonian is formally equivalent to a modified Dirac equation with altermagnetic mass, where $\Delta(k_z)$ serves as a k_z -dependent Dirac mass term. The bulk spectrum is given by

$$E(\mathbf{k}) = -t(\cos k_x + \cos k_y) \pm \sqrt{\lambda^2(\sin^2 k_x + \sin^2 k_y) + M(\mathbf{k})^2}. \quad (12)$$

Bulk gap closings require $\sin k_x = \sin k_y = 0$ and $M(\mathbf{k}) = 0$ are satisfied. The first condition restricts (k_x, k_y) to $(0, 0)$, $(0, \pi)$, $(\pi, 0)$, (π, π) . At $(0, 0)$ and (π, π) , since $\cos k_y - \cos k_x = 0$, the mass term reduces to $M = \pm \Delta(k_z)$. Thus, gap closing requires $\Delta(k_z) = 0$. According to Eq. (9), the condition is given by

$$\cos(k_z d) = -\frac{\Delta_S^2 + \Delta_D^2}{2 \Delta_S \Delta_D}. \quad (13)$$

A real solution for k_z exists only when the right-hand side is within $[-1, 1]$, i.e., when $\Delta_S = \Delta_D$. Therefore, for generic parameters, these degeneracies are lifted and the system remains gapped at these points.

At the points $(0, \pi)$ and $(\pi, 0)$, where $\cos k_y - \cos k_x = \pm 2$, the mass term becomes $M = \pm 2J \pm \Delta(k_z)$. The gapless condition then reads

$$\Delta(k_z) = \mp 2J, \quad (14)$$

which gives

$$\Delta_S^2 + \Delta_D^2 + 2\Delta_S\Delta_D \cos(k_z d) = 4J^2, \quad (15)$$

and hence

$$\cos(k_z d) = \frac{4J^2 - (\Delta_S^2 + \Delta_D^2)}{2\Delta_S\Delta_D}. \quad (16)$$

The existence of real solutions requires

$$-1 \leq \frac{4J^2 - (\Delta_S^2 + \Delta_D^2)}{2\Delta_S\Delta_D} \leq 1, \quad (17)$$

or equivalently,

$$\frac{(\Delta_S - \Delta_D)^2}{4} \leq J^2 \leq \frac{(\Delta_S + \Delta_D)^2}{4}. \quad (18)$$

Introducing the notations

$$J_{c1} = \frac{|\Delta_S - \Delta_D|}{2}, \quad J_{c2} = \frac{\Delta_S + \Delta_D}{2}, \quad (19)$$

we find that Weyl nodes exist only within the parameter window

$$J_{c1} \leq J \leq J_{c2}. \quad (20)$$

In this regime, Eq. (14) admits two real solutions for each of the points $(0, \pi)$ and $(\pi, 0)$, corresponding to distinct values of k_z . Thus, a total of four Weyl nodes emerge at positions $(0, \pi, \pm k_z^c)$ and $(\pi, 0, \pm k_z^c)$, each set forming a pair of nodes with opposite chirality, as required by the Nielsen–Ninomiya theorem [16, 59]. Here, k_z^c is given by

$$k_z^c = \frac{1}{d} \arccos \left(\frac{4J^2 - (\Delta_S^2 + \Delta_D^2)}{2\Delta_S\Delta_D} \right).$$

With the above analysis, we clearly outline the topological phase diagram at fixed altermagnetic exchange parameter $J = 0.5$, as shown in Fig. 3(b). The diagram features three distinct topological regions, defined by the tunneling parameters Δ_S and Δ_D .

For sufficiently large differences ($|\Delta_S - \Delta_D| > 2J$), the system is fully gapped and trivial, as dominant tunneling prevents band inversion. Conversely, in the intermediate regime ($|\Delta_S - \Delta_D| < 2J \leq \Delta_S + \Delta_D$), Weyl nodes appear, forming a Weyl semimetal phase. These nodes persist until the critical boundaries ($|\Delta_S - \Delta_D| = 2J$ or

$\Delta_S + \Delta_D = 2J$) where they annihilate pairwise at the Brillouin zone edge, signaling a topological transition.

Finally, when $\Delta_S + \Delta_D < 2J$, the system transitions to a 3D quantum spin Hall (QSH) insulator phase, with robust helical surface states throughout the Brillouin zone. This phase is distinct from the trivial insulator and Weyl semimetal phases.

Figure 4 demonstrates the topological evolution across these phases as the intra-layer tunneling parameter Δ_S is varied. Panels (a)–(c) show the Fermi surface contours for the three representative parameter sets [corresponding to points I–III in Fig. 3(b)], directly visualizing the sequence from the 3D QSH phase, through the Weyl semimetal, to the trivial insulator.

In the Weyl semimetal phase [Fig. 4(b)], the bulk band structure hosts two pairs of Weyl nodes located at $(k_x, k_y, k_z) = (0, -\pi, \pm k_z^c)$ and $(\pi, 0, \pm k_z^c)$, where k_z^c denotes their positions along the k_z -axis. The separation and location of these Weyl nodes are primarily controlled by Δ_S . As Δ_S increases, the Weyl nodes move toward the Brillouin zone boundaries at $k_z = \pm\pi$ [Fig. 4(c)], eventually annihilating in pairs of opposite chirality at these boundaries, driving the system into a trivial insulating phase. Conversely, decreasing Δ_S shifts the Weyl nodes toward the $k_z = 0$ plane. At a critical Δ_S value [Fig. 4(a)], the Weyl nodes merge into Dirac points at $(0, -\pi, 0)$ and $(\pi, 0, 0)$, and additional gapless points emerge simultaneously at other high-symmetry momenta $(0, 0, \pm\pi)$ and $(\pi, -\pi, \pm\pi)$. Further decreasing Δ_S re-opens a full bulk gap without any Weyl nodes, leading the system into a three-dimensional quantum spin Hall insulating phase characterized by robust topological surface states, as discussed below.

Here, a key signature of the altermagnetic Weyl semimetal is the emergence of helical Fermi arcs on the side surfaces, in contrast to the single chiral arc seen in conventional Weyl semimetals [1, 2]. In this context, the term helical Fermi arcs denotes a pair of counter-propagating surface states with opposite group velocities on the same surface, rather than spin–momentum locking. To demonstrate this, we perform a slab calculation, taking the system finite along the x direction and infinite along y and z . The calculated surface band structure [Fig. 4(d1)–(d5)] shows that, between the two Weyl nodes at $k_z = \pm k_z^c$, the bulk gap remains open, but in-gap states localized on the surfaces appear. These surface states, color-coded by position, form Fermi arcs that traverse the gap and connect the projections of the Weyl nodes. Crucially, on the same surface, Fermi arcs with opposite group velocities coexist, so their net chirality vanishes. The emergence of such helical Fermi arcs arises from the interplay between the Dirac mass and the altermagnetic mass. Specifically, the two blocks of the Hamiltonian share the same altermagnetic mass but have Dirac masses of opposite sign, leading to opposite Chern numbers in the two blocks. As a result, on the surface, coexisting Fermi arcs with opposite chirality are generated, which is a hallmark feature of the altermag-

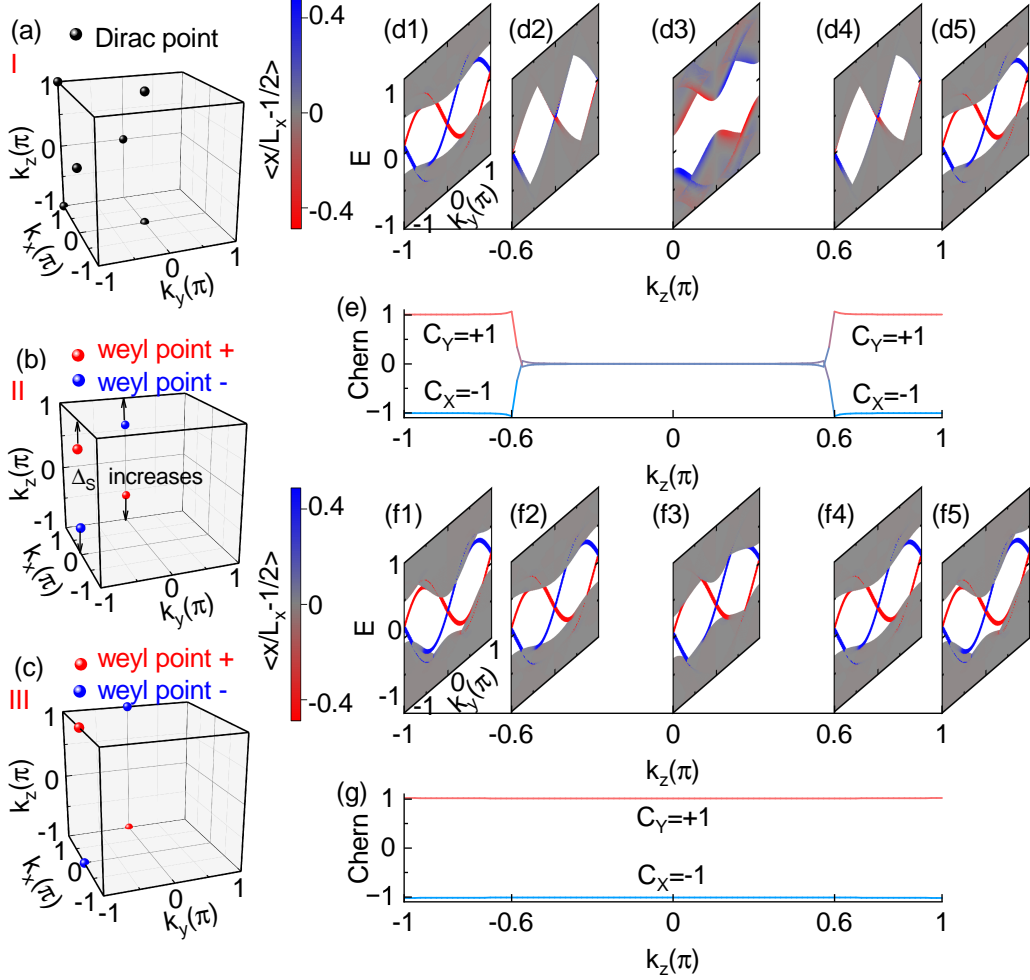


FIG. 4. (a–c) Fermi surface distributions for three representative parameter sets, marked by points I, II, and III in Fig. 3(b). (d1–d5) Slab spectra as a function of k_z in the Weyl semimetal phase with $\Delta D = 0.5$ and $\Delta S = 1$, with eigenstates color-coded by their average position $\langle x \rangle$. (e) The corresponding Chern number $C(k_z)$, which exhibits a jump at the Weyl nodes. (f1–f5) Slab spectra as a function of k_z in the QSH phase with $\Delta D = 0.5$ and $\Delta S = 0.2$, again color-coded by average position. (g) The corresponding Chern number $C(k_z)$, remaining constant throughout, consistent with robust QSH edge states and the absence of Weyl nodes.

netic Weyl phase.

This momentum-space distribution of Fermi arcs is intimately linked to the partial Chern numbers defined at high-symmetry points in each k_z slice. For every fixed k_z , the effective two-dimensional Hamiltonian takes the form of a modified Dirac equation with an altermagnetic mass term. Due to inversion symmetry, the topological structure can be further refined by considering skyrmion charges at the high-symmetry points $(0, \pi)$ and $(\pi, 0)$ [56]. Considering that the Dirac mass terms have opposite sign in the two blocks of the Hamiltonian, their interplay with the altermagnetic mass leads to partial Chern numbers $C_X = -1$ and $C_Y = +1$ at the respective high-symmetry points. This structure directly dictates the existence of counter-propagating Fermi arcs: boundary modes associated with $C_X = -1$ appear near $k_y \approx 0$, while those with $C_Y = +1$ localize near $k_y \approx \pi$. The opposite signs

set their chirality, and the association with different high-symmetry points ensures the robustness and coexistence of these paired arcs on the same surface against long-range disorder[56, 60]. In particular, after the unitary transformation $U = e^{i\pi\sigma_z\tau_z/4}$, the Hamiltonian becomes block-diagonal, revealing an emergent layer–spin locking symmetry that ties the spin orientation to the layer index and prevents hybridization between the two sectors in the ideal limit. Moreover, even when a weak inter-block coupling is introduced, the Fermi arcs remain gapless because they originate from distinct high-symmetry points carrying localized topological charges ($C_X = -1$, $C_Y = +1$) that cannot annihilate or mix. Therefore, both of the layer–spin locking symmetry and high-symmetry-point Chern protection ensure the stability of the helical surface states. The evolution of these topological features as a function of k_z is further reflected in the cal-

culated Chern number $C(k_z)$ for each two-dimensional k_x - k_y slice [Fig. 4(e)]. In the Weyl phase, $C(k_z)$ undergoes quantized jumps of ± 1 as k_z crosses each Weyl node, but the total Chern number always vanishes because the two blocks of the Hamiltonian experience opposite changes. This distribution of partial Chern numbers underlies the coexistence of helical Fermi arcs and defines the unique topological nature of the altermagnetic Weyl semimetal.

Upon further decreasing Δ_S , the Weyl nodes move toward the $k_z = 0$ plane and eventually annihilate, driving the system into a three-dimensional QSH phase [Fig. 4(a)]. In this regime, the Chern numbers of each block remain fixed for all k_z [Fig. 4(g)], and robust helical edge states persist throughout the Brillouin zone [Figs. 4(f1)–4(f5)]. Thus, by tuning system parameters, a sequence of topological phase transitions is induced, with the interplay between the Dirac and altermagnetic masses giving rise to the emergence of paired Weyl nodes, helical Fermi arcs, and ultimately a strong QSH phase. This progression highlights the unique bulk-boundary correspondence and the rich topological phase diagram enabled by altermagnetic order.

V. SUMMARY

In summary, we have demonstrated that the introduction of an altermagnetic mass in a modified Dirac Hamiltonian leads to a distinctive Weyl semimetal phase, fundamentally different from the conventional Wilson mass scenario. The altermagnetic mass drives transitions between nontrivial topological phases by shifting the location of topological charge among high-symmetry points, resulting in pairs of Weyl nodes and the coexistence of helical Fermi arcs with opposite chirality on the same surface. Our minimal lattice model, supported by explicit calculations of bulk and surface spectra, Berry curvature, and Chern numbers, reveals a rich topological phase diagram including trivial insulator, Weyl semimetal, and quantum spin Hall phases. Finally, we propose that multilayer structures composed of 2D Rashba metal and insulating spacers offer a platform for realizing altermagnetic Weyl semimetals. Our results illuminate the rich topological physics accessible via altermagnetism, clarify the unique impact of the altermagnetic mass term on Dirac band topology, and provide concrete guidelines for the experimental realization and detection of altermagnetic Weyl semimetals.

ACKNOWLEDGEMENTS

This work was financially supported by the National Key R and D Program of China (Grant No. 2024YFA1409002), the National Natural Science Foundation of China (Grants No. 12374034, Grants No. 124B2069, and Grants No. 12447147), the Quantum Science and Technology-National Science and Technology Major Project (Grant No. 2021ZD0302403), and the China Postdoctoral Science Foundation (Grant No. 2024M760070). The computational resources are supported by the High-Performance Computing Platform of Peking University.

dation of China (Grants No. 12374034, Grants No. 124B2069, and Grants No. 12447147), the Quantum Science and Technology-National Science and Technology Major Project (Grant No. 2021ZD0302403), and the China Postdoctoral Science Foundation (Grant No. 2024M760070). The computational resources are supported by the High-Performance Computing Platform of Peking University.

APPENDIX: $\mathcal{C}_6\mathcal{T}$ -SYMMETRIC ALTERMAGNETIC MASS AND DIRAC TOPOLOGY

Recent theoretical and experimental studies have identified MnTe as a representative g -wave altermagnet [25], whose momentum-dependent Zeeman splitting in the $k_z > 0$ sector respects the combined $\mathcal{C}_6\mathcal{T}$ symmetry. By placing a two-dimensional Rashba metal in proximity to such a g -wave altermagnet, one can induce an effective $\mathcal{C}_6\mathcal{T}$ -symmetric altermagnetic mass term via interfacial exchange coupling or magnetic proximity effect. Notably, this effective mass term takes the same functional form as the two-dimensional f -wave magnetic order, which can naturally exist on hexagonal-like lattices [61].

To directly examine the topological effect of the $\mathcal{C}_6\mathcal{T}$ -symmetric altermagnetic mass, we consider a Dirac Hamiltonian on a hexagonal lattice with a conventional Dirac mass m_0 and an altermagnetic mass of strength J :

$$H^h(\mathbf{k}) = \sum_{i=1}^3 v_F \sin(\mathbf{k} \cdot \mathbf{a}_i) [(\hat{\mathbf{a}}_i \cdot \hat{x})\sigma_x + (\hat{\mathbf{a}}_i \cdot \hat{y})\sigma_y] + \left\{ m_0 + J \left[\sum_{i=1}^3 \sin(\mathbf{k} \cdot \mathbf{a}_i) \right] \right\} \sigma_z. \quad (21)$$

Here, the nearest-neighbor bond vectors are $\mathbf{a}_1 = (1, 0)$, $\mathbf{a}_2 = (-1, \sqrt{3})/2$, and $\mathbf{a}_3 = (-1, -\sqrt{3})/2$ (the lattice constant is set to unity).

For this two-band Hamiltonian $H(\mathbf{k}) = \mathbf{d}(\mathbf{k}) \cdot \boldsymbol{\sigma}$, the vector $\mathbf{d}(\mathbf{k}) = (d_x, d_y, d_z)$ defines a mapping from the Brillouin zone to the Bloch sphere, which encodes the topological character of the band structure and is directly related to the Chern number.

As shown in Fig. 5(a,b), the $\mathbf{d}(\mathbf{k})$ textures for opposite mass signs ($m_0 = \pm 1$) exhibit band-inversion surfaces enclosing the K and K' points, respectively. From these textures, one finds that the two Dirac sectors carry opposite Chern numbers, $C_K = +1$ and $C_{K'} = -1$, confirming that the sign reversal of the Dirac mass drives a Chern-number inversion—exactly as in the d -wave case discussed in the main text. This demonstrates that the same topological mechanism applies to altermagnetic masses with different form factors, including those with $\mathcal{C}_6\mathcal{T}$ symmetry.

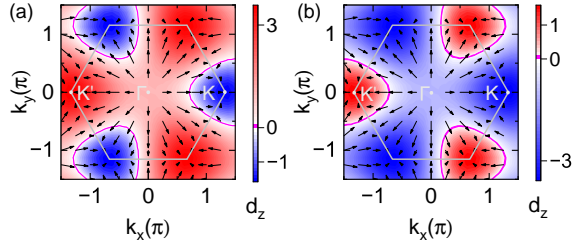


FIG. 5. (a,b) Momentum-space textures of $\mathbf{d}(\mathbf{k}) = (d_x, d_y, d_z)$ for the hexagonal-lattice model with Dirac masses $m_0 = \pm 1$, $v_F = 1$, and $J = 1$. The band-inversion surfaces defined by $d_z(\mathbf{k}) = 0$ enclose the K and K' valleys for opposite mass signs

[1] X. Wan, A. M. Turner, A. Vishwanath, and S. Y. Savrasov, Topological semimetal and Fermi-arc surface states in the electronic structure of pyrochlore iridates, *Phys. Rev. B* **83**, 205101 (2011).

[2] N. P. Armitage, E. J. Mele, and A. Vishwanath, Weyl and Dirac semimetals in three-dimensional solids, *Rev. Mod. Phys.* **90**, 015001 (2018).

[3] Shuichi Murakami, Phase transition between the quantum spin Hall and insulator phases in 3D: emergence of a topological gapless phase, *New Journal of Physics* **9**, 356 (2007).

[4] G. B. Halász and L. Balents, Time-reversal invariant realization of the Weyl semimetal phase, *Phys. Rev. B* **85**, 035103 (2012).

[5] S. Fan, B. Fu, D.-S. Ma, and R. Wang, Complete topological phase diagram and realization of minimum Weyl nodes in a sheared chiral crystal of elemental tellurium, *Phys. Rev. B* **108**, 235211 (2023).

[6] A. A. Burkov and L. Balents, Weyl Semimetal in a Topological Insulator Multilayer, *Phys. Rev. Lett.* **107**, 127205 (2011).

[7] E. Liu, Y. Sun, N. Kumar, L. Muechler, A. Sun, L. Jiao, S.-Y. Yang, D. Liu, A. Liang, Q. Xu, J. Kroder, V. Süß, H. Borrman, C. Shekhar, Z. Wang, C. Xi, W. Wang, W. Schnelle, S. Wirth, Y. Chen, S. T. B. Goennenwein, and C. Felser, Giant anomalous Hall effect in a ferromagnetic kagome-lattice semimetal, *Nature Physics* **14**, 1125 (2018).

[8] Z. Wang, M. G. Vergniory, S. Kushwaha, M. Hirschberger, E. V. Chulkov, A. Ernst, N. P. Ong, R. J. Cava, and B. A. Bernevig, Time-Reversal-Breaking Weyl Fermions in Magnetic Heusler Alloys, *Phys. Rev. Lett.* **117**, 236401 (2016).

[9] S. Nie, T. Hashimoto, and F. B. Prinz, Magnetic Weyl Semimetal in $K_2Mn_3(AsO_4)_3$ with the Minimum Number of Weyl Points, *Phys. Rev. Lett.* **128**, 176401 (2022).

[10] S. Fan, S. Huang, Z. Chen, F. Zhan, X.-Y. Ding, D.-S. Ma, and R. Wang, Circularly polarized light irradiated ferromagnetic $MnBi_2Te_4$: A possible ideal Weyl semimetal, *Phys. Rev. B* **110**, 125204 (2024).

[11] K. Kuroda, T. Tomita, M.-T. Suzuki, C. Bareille, A. Nugroho, P. Goswami, M. Ochi, M. Ikhlas, M. Nakayama, S. Akebi, R. Noguchi, R. Ishii, N. Inami, K. Ono, H. Kumigashira, A. Varykhalov, T. Muro, T. Koretsune, R. Arita, S. Shin, T. Kondo, and S. Nakatsuji, Evidence for magnetic Weyl fermions in a correlated metal, *Nature Materials* **16**, 1090 (2017).

[12] D. Grassano, L. Binci, and N. Marzari, Type-I antiferromagnetic Weyl semimetal $InMnTi_2$, *Phys. Rev. Res.* **6**, 013140 (2024).

[13] A. A. Burkov, Anomalous Hall Effect in Weyl Metals, *Phys. Rev. Lett.* **113**, 187202 (2014).

[14] A. A. Burkov, Chiral anomaly and transport in Weyl metals, *Journal of Physics: Condensed Matter* **27**, 113201 (2015).

[15] S. Itoh, Y. Endoh, T. Yokoo, S. Ibuka, J.-G. Park, Y. Kaneko, K. S. Takahashi, Y. Tokura, and N. Nagaosa, Weyl fermions and spin dynamics of metallic ferromagnet $SrRuO_3$, *Nature Communications* **7**, 11788 (2016).

[16] H. Nielsen and M. Ninomiya, The Adler-Bell-Jackiw anomaly and Weyl fermions in a crystal, *Physics Letters B* **130**, 389 (1983).

[17] V. Aji, Adler-Bell-Jackiw anomaly in Weyl semimetals: Application to pyrochlore iridates, *Phys. Rev. B* **85**, 241101 (2012).

[18] C.-X. Liu, P. Ye, and X.-L. Qi, Chiral gauge field and axial anomaly in a Weyl semimetal, *Phys. Rev. B* **87**, 235306 (2013).

[19] Q.-D. Jiang, H. Jiang, H. Liu, Q.-F. Sun, and X. C. Xie, Topological imbert-fedorov shift in Weyl semimetals, *Phys. Rev. Lett.* **115**, 156602 (2015).

[20] Z. Hou and Q.-F. Sun, Nonlocal correlation mediated by Weyl orbits, *Phys. Rev. Res.* **2**, 023236 (2020).

[21] N. Morali, R. Batabyal, P. K. Nag, E. Liu, Q. Xu, Y. Sun, B. Yan, C. Felser, N. Avraham, and H. Beidenkopf, Fermi-arc diversity on surface terminations of the magnetic Weyl semimetal $Co_3Sn_2S_2$, *Science* **365**, 1286 (2019).

[22] S. Ma, Y. Bi, Q. Guo, B. Yang, O. You, J. Feng, H.-B. Sun, and S. Zhang, Linked Weyl surfaces and Weyl arcs in photonic metamaterials, *Science* **373**, 572 (2021).

[23] X. Zheng, Q. Gu, Y. Liu, B. Tong, J.-F. Zhang, C. Zhang, S. Jia, J. Feng, and R.-R. Du, Observation of 1D Fermi arc states in Weyl semimetal TaAs, *National Science Review* **9**, nwab191 (2022).

[24] L. Šmejkal, R. González-H., T. Jungwirth, and J. Sinova, Crystal time-reversal symmetry breaking and spontaneous Hall effect in collinear antiferromagnets, *Science Advances* **6**, eaaz8809 (2020).

[25] J. Krempaský, L. Šmejkal, S. W. D’Souza, M. Hajaoui, G. Springholz, K. Uhlířová, F. Alarab, P. C. Constantinou, V. Strocov, D. Usanov, W. R. Pudelko, R. González-Hernández, A. Birk Hellenes, Z. Jansa, H. Reichlová, Z. Šobáň, R. D. Gonzalez Betancourt, P. Wadley, J. Sinova, D. Kriegner, J. Minár, J. H. Dil, and T. Jungwirth, Altermagnetic lifting of Kramers spin degeneracy, *Nature* **626**, 517 (2024).

[26] C. Song, H. Bai, Z. Zhou, L. Han, H. Reichlova, J. H. Dil, J. Liu, X. Chen, and F. Pan, Altermagnets as a new class of functional materials, *Nature Reviews Materials* **10**, 473 (2025).

[27] Z.-M. Wang, Y. Zhang, S.-B. Zhang, J.-H. Sun, E. Dagotto, D.-H. Xu, and L.-H. Hu, Spin-orbital altermagnetism, *Phys. Rev. Lett.* **135**, 176705 (2025).

[28] L. Šmejkal, J. Sinova, and T. Jungwirth, Beyond Conventional Ferromagnetism and Antiferromagnetism: A Phase with Nonrelativistic Spin and Crystal Rotation Symmetry, *Phys. Rev. X* **12**, 031042 (2022).

[29] L. Šmejkal, J. Sinova, and T. Jungwirth, Emerging Research Landscape of Altermagnetism, *Phys. Rev. X* **12**, 040501 (2022).

[30] H. Bai, L. Han, X. Y. Feng, Y. J. Zhou, R. X. Su, Q. Wang, L. Y. Liao, W. X. Zhu, X. Z. Chen, F. Pan, X. L. Fan, and C. Song, Observation of Spin Splitting Torque in a Collinear Antiferromagnet RuO₂, *Phys. Rev. Lett.* **128**, 197202 (2022).

[31] S. Karube, T. Tanaka, D. Sugawara, N. Kadoguchi, M. Kohda, and J. Nitta, Observation of Spin-Splitter Torque in Collinear Antiferromagnetic RuO₂, *Phys. Rev. Lett.* **129**, 137201 (2022).

[32] L. Šmejkal, A. B. Hellenes, R. González-Hernández, J. Sinova, and T. Jungwirth, Giant and Tunneling Magnetoresistance in Unconventional Collinear Antiferromagnets with Nonrelativistic Spin-Momentum Coupling, *Phys. Rev. X* **12**, 011028 (2022).

[33] R. González-Hernández, L. Šmejkal, K. Výborný, Y. Yaghgi, J. Sinova, T. Jungwirth, and J. Železný, Efficient Electrical Spin Splitter Based on Nonrelativistic Collinear Antiferromagnetism, *Phys. Rev. Lett.* **126**, 127701 (2021).

[34] X.-J. Yi, Y. Mao, X. Lu, and Q.-F. Sun, Spin splitting Nernst effect in altermagnets, *Phys. Rev. B* **111**, 035423 (2025).

[35] Y.-H. Wan and Q.-F. Sun, Altermagnetism-induced parity anomaly in weak topological insulators, *Phys. Rev. B* **111**, 045407 (2025).

[36] R. Chen, X.-X. Yi, B. Zhou, and D.-H. Xu, Anomalous Hall effects in magnetic weak topological insulator films, *Physical Review B* **111**, 10.1103/PhysRevB.111.045409 (2025).

[37] W. Chen, X. Zhou, W.-K. Lou, and K. Chang, Magneto-optical conductivity and circular dichroism in *d*-wave altermagnets, *Phys. Rev. B* **111**, 064428 (2025).

[38] D. Zhu, D. Liu, Z.-Y. Zhuang, Z. Wu, and Z. Yan, Field-sensitive dislocation bound states in two-dimensional *d*-wave altermagnets, *Phys. Rev. B* **110**, 165141 (2024).

[39] R. Chen, Z.-M. Wang, K. Wu, H.-P. Sun, B. Zhou, R. Wang, and D.-H. Xu, Probing *k*-space alternating spin polarization via the anomalous hall effect, *Phys. Rev. Lett.* **135**, 096602 (2025).

[40] L. Liu, C.-M. Miao, Q.-F. Sun, and Y.-T. Zhang, Quantum spin hall effect in bilayer honeycomb lattices with *c*-type antiferromagnetic order, *Phys. Rev. B* **111**, 165421 (2025).

[41] L. Liu, Q.-F. Sun, and Y.-T. Zhang, Tunable two-dimensional dirac-weyl semimetal phase induced by altermagnetism, *Phys. Rev. B* **112**, L161411 (2025).

[42] J. A. Ouassou, A. Brataas, and J. Linder, dc Josephson Effect in Altermagnets, *Phys. Rev. Lett.* **131**, 076003 (2023).

[43] D. Zhu, Z.-Y. Zhuang, Z. Wu, and Z. Yan, Topological superconductivity in two-dimensional altermagnetic metals, *Phys. Rev. B* **108**, 184505 (2023).

[44] Q. Cheng and Q.-F. Sun, Orientation-dependent Josephson effect in spin-singlet superconductor/altermagnet/spin-triplet superconductor junctions, *Phys. Rev. B* **109**, 024517 (2024).

[45] Q. Cheng, Y. Mao, and Q.-F. Sun, Field-free Josephson diode effect in altermagnet/normal metal/altermagnet junctions, *Phys. Rev. B* **110**, 014518 (2024).

[46] S. Banerjee and M. S. Scheurer, Altermagnetic superconducting diode effect, *Phys. Rev. B* **110**, 024503 (2024).

[47] P. Chatterjee and V. Jurić, Interplay between altermagnetism and topological superconductivity on an unconventional superconducting platform, *Phys. Rev. B* **112**, 054503 (2025).

[48] S.-Q. Shen, *Topological Insulators: Dirac Equation in Condensed Matters*, Springer Series in Solid-State Sciences, Vol. 174 (Springer Berlin Heidelberg, Berlin, Heidelberg, 2012).

[49] X.-L. Qi, Y.-S. Wu, and S.-C. Zhang, Topological quantization of the spin Hall effect in two-dimensional paramagnetic semiconductors, *Phys. Rev. B* **74**, 085308 (2006).

[50] B. A. Bernevig, T. L. Hughes, and S.-C. Zhang, Quantum Spin Hall Effect and Topological Phase Transition in HgTe Quantum Wells, *Science* **314**, 1757 (2006).

[51] H. Zhang, C.-X. Liu, X.-L. Qi, X. Dai, Z. Fang, and S.-C. Zhang, Topological insulators in Bi₂Se₃, Bi₂Te₃ and Sb₂Te₃ with a single Dirac cone on the surface, *Nature Physics* **5**, 438 (2009).

[52] Y.-H. Wan, P.-Y. Liu, and Q.-F. Sun, Interplay of altermagnetic order and wilson mass in the dirac equation: Helical edge states without time-reversal symmetry, *Phys. Rev. B* **112**, 115412 (2025).

[53] J. Kogut and L. Susskind, Hamiltonian formulation of Wilson’s lattice gauge theories, *Phys. Rev. D* **11**, 395 (1975).

[54] H. J. Rothe, *Lattice Gauge Theories: An Introduction*, 4th ed., World Scientific Lecture Notes in Physics (WORLD SCIENTIFIC, 2012).

[55] B. Fu, J.-Y. Zou, Z.-A. Hu, H.-W. Wang, and S.-Q. Shen, Quantum anomalous semimetals, *npj Quantum Materials* **7**, 94 (2022).

[56] Y.-H. Wan, P.-Y. Liu, and Q.-F. Sun, Classification of Chern numbers based on high-symmetry points, *Phys. Rev. B* **111**, L161410 (2025).

[57] O. Fedchenko, J. Minár, A. Akashdeep, S. W. D’Souza, D. Vasilyev, O. Tkach, L. Odenbreit, Q. Nguyen, D. Kurnyakhov, N. Wind, L. Wenthaus, M. Scholz, K. Rossnagel, M. Hoesch, M. Aeschlimann, B. Stadtmüller, M. Kläui, G. Schönhense, T. Jungwirth, A. B. Hellenes, G. Jakob, L. Šmejkal, J. Sinova, and H.-J. Elmers, Observation of time-reversal symmetry breaking in the band

structure of altermagnetic ruo₂, *Sci. Adv.* **10**, eadj4883 (2024).

[58] B. Jiang, M. Hu, J. Bai, Z. Song, C. Mu, G. Qu, W. Li, W. Zhu, H. Pi, Z. Wei, Y.-J. Sun, Y. Huang, X. Zheng, Y. Peng, L. He, S. Li, J. Luo, Z. Li, G. Chen, H. Li, H. Weng, and T. Qian, A metallic room-temperature d-wave altermagnet, *Nat. Phys.* **21**, 754 (2025).

[59] H. Nielsen and M. Ninomiya, A no-go theorem for regularizing chiral fermions, *Physics Letters B* **105**, 219 (1981).

[60] H. Li, H. Jiang, Q.-F. Sun, and X. Xie, Emergent energy dissipation in quantum limit, *Science Bulletin* **69**, 1221 (2024).

[61] S. Hayami, Y. Yanagi, and H. Kusunose, Bottom-up design of spin-split and reshaped electronic band structures in antiferromagnets without spin-orbit coupling: Procedure on the basis of augmented multipoles, *Phys. Rev. B* **102**, 144441 (2020).